First Direct Detection Constraints on Planck-Scale Mass Dark Matter with Multiple-Scatter Signatures Using the DEAP-3600 Detector

P. Adhikari,[5] R. Ajaj,[5,25] M. Alpízar-Venegas,[13] D. J. Auty,[1] H. Benmansour,[19] C. E. Bina,[1,25] W. Bonivento,[9] M. G. Boulay,[5] M. Cadeddu,[3,9] B. Cai,[5,25] M. Cárdenas-Montes,[6] S. Cavuoti,[8,7,11] Y. Chen,[1] B. T. Cleveland,[21,12] J. M. Corning,[19] S. Daugherty,[12] P. DelGobbo,[5,25] P. Di Stefano,[19] L. Doria,[18] M. Dunford,[5] E. Ellingwood,[19] A. Erlandson,[5,4] S. S. Farahani,[1] N. Fatemighomi,[21,20] G. Fiorillo,[7,11] D. Gallacher,[5] P. García Abia,[6] S. Garg,[5] P. Giampa,[23] D. Goeldi,[5,25] P. Gorel,[21,12,25] K. Graham,[5] A. Grobov,[15,16] A. L. Hallin,[1] M. Hamstra,[5] T. Hugues,[2] A. Ilyasov,[15,16] A. Joy,[1,25] B. Jigmeddorj,[4] C. J. Jillings,[21,12] O. Kamaev,[4] G. Kaur,[5] A. Kemp,[19,20] I. Kochanek,[10] M. Kuźniak,[2,5,25] M. Lai,[3,9] S. Langrock,[12,25] B. Lehnert,[5,*] A. Leonhardt,[24] N. Levashko,[15,16] X. Li,[17] M. Lissia,[9] O. Litvinov,[23] J. Lock,[5] G. Longo,[7,11] I. Machulin,[15,16] A. B. McDonald,[19] T. McElroy,[1] J. B. McLaughlin,[20,23] C. Mielnichuk,[1] L. Mirasola,[3] J. Monroe,[20] G. Oliviéro,[5,25] S. Pal,[1,25] S. J. M. Peeters,[22] M. Perry,[5] V. Pesudo,[6] E. Picciau,[9,3] M.-C. Piro,[1,25] T. R. Pollmann,[24,†] N. Raj,[23] E. T. Rand,[4] C. Rethmeier,[5] F. Retière,[23] I. Rodríguez-García,[6] L. Roszkowski,[2,14] J. B. Ruhland,[24] E. Sanchez García,[6] T. Sánchez-Pastor,[6] R. Santorelli,[6] S. Seth,[5,25] D. Sinclair,[5] P. Skensved,[19] B. Smith,[23] N. J. T. Smith,[21,12] T. Sonley,[21,25] R. Stainforth,[5] M. Stringer,[19,25] B. Sur,[4] E. Vázquez-Jáuregui,[13,12] S. Viel,[5,25] J. Walding,[20] M. Waqar,[5,25] M. Ward,[19,21] S. Westerdale,[9,5] J. Willis,[1] and A. Zuñiga-Reyes[13]

(DEAP Collaboration)[‡]

[1]*Department of Physics, University of Alberta, Edmonton, Alberta, T6G 2R3, Canada*
[2]*AstroCeNT, Nicolaus Copernicus Astronomical Center, Polish Academy of Sciences, Rektorska 4, 00-614 Warsaw, Poland*
[3]*Physics Department, Università degli Studi di Cagliari, Cagliari 09042, Italy*
[4]*Canadian Nuclear Laboratories, Chalk River, Ontario, K0J 1J0, Canada*
[5]*Department of Physics, Carleton University, Ottawa, Ontario, K1S 5B6, Canada*
[6]*Centro de Investigaciones Energéticas, Medioambientales y Tecnológicas, Madrid 28040, Spain*
[7]*Physics Department, Università degli Studi "Federico II" di Napoli, Napoli 80126, Italy*
[8]*Astronomical Observatory of Capodimonte, Salita Moiariello 16, I-80131 Napoli, Italy*
[9]*INFN Cagliari, Cagliari 09042, Italy*
[10]*INFN Laboratori Nazionali del Gran Sasso, Assergi (AQ) 67100, Italy*
[11]*INFN Napoli, Napoli 80126, Italy*
[12]*Department of Physics and Astronomy, Laurentian University, Sudbury, Ontario, P3E 2C6, Canada*
[13]*Instituto de Física, Universidad Nacional Autónoma de México, A.P. 20-364, México D.F. 01000, México*
[14]*BP2, National Centre for Nuclear Research, ul. Pasteura 7, 02-093 Warsaw, Poland*
[15]*National Research Centre Kurchatov Institute, Moscow 123182, Russia*
[16]*National Research Nuclear University MEPhI, Moscow 115409, Russia*
[17]*Physics Department, Princeton University, Princeton, New Jersey 08544, USA*
[18]*PRISMA$^+$, Cluster of Excellence and Institut für Kernphysik, Johannes Gutenberg-Universität Mainz, 55128 Mainz, Germany*
[19]*Department of Physics, Engineering Physics, and Astronomy, Queen's University, Kingston, Ontario, K7L 3N6, Canada*
[20]*Royal Holloway University London, Egham Hill, Egham, Surrey TW20 0EX, United Kingdom*
[21]*SNOLAB, Lively, Ontario, P3Y 1N2, Canada*
[22]*University of Sussex, Sussex House, Brighton, East Sussex BN1 9RH, United Kingdom*
[23]*TRIUMF, Vancouver, British Columbia, V6T 2A3, Canada*
[24]*Department of Physics, Technische Universität München, 80333 Munich, Germany*
[25]*Arthur B. McDonald Canadian Astroparticle Physics Research Institute, Queen's University, Kingston ON K7L 3N6,Canada*

(Received 25 August 2021; revised 15 October 2021; accepted 16 November 2021; published 5 January 2022)

Dark matter with Planck-scale mass ($\simeq 10^{19}$ GeV$/c^2$) arises in well-motivated theories and could be produced by several cosmological mechanisms. A search for multiscatter signals from supermassive dark matter was performed with a blind analysis of data collected over a 813 d live time with DEAP-3600, a 3.3 t single-phase liquid argon-based detector at SNOLAB. No candidate signals were observed, leading to the

first direct detection constraints on Planck-scale mass dark matter. Leading limits constrain dark matter masses between 8.3×10^6 and 1.2×10^{19} GeV/c^2, and ^{40}Ar-scattering cross sections between 1.0×10^{-23} and 2.4×10^{-18} cm^2. These results are interpreted as constraints on composite dark matter models with two different nucleon-to-nuclear cross section scalings.

DOI: 10.1103/PhysRevLett.128.011801

Introduction.—Despite the abundance of dark matter (DM) [1], little is known about its particle nature. While weakly interacting massive particles (WIMPs) of electroweak masses and possible thermal origin are promising candidates and are the subject of several recent searches (e.g., Refs. [2–8], also Ref. [9]), other well-motivated candidates span many orders of magnitude in mass and may evade current constraints.

DM with Planck-scale mass ($m_\chi \simeq 10^{19}$ GeV/c^2) may be produced nonthermally, such as in inflaton decay or gravitational mechanisms related to inflation [10–14], often related to grand unified theories. Other models describe superheavy DM produced by primordial black hole radiation [15] or extended thermal production in a dark sector [16].

Direct detection constraints at these masses are limited by the DM number density rather than the cross section. As a result, even large cross sections permitting multiple scatters remain unconstrained. While the finite overburden may allow sufficiently massive particles to be detected underground [17], typical WIMP analyses that reject pileup and multiple-scatter signatures cannot be extrapolated to these high cross sections. Instead, dedicated analyses are required [17–19], which can probe a variety of theoretical scenarios giving superheavy, stable, and strongly interacting states [18,20–25].

Previous direct detection searches constrain DM with $m_\chi \lesssim 6 \times 10^{17}$ GeV/c^2 [26–30]. The present study uses data taken with DEAP-3600, 2 km underground at SNOLAB, to probe m_χ up to the Planck scale using multiple-scatter signals, placing the first direct detection constraints at these masses.

Detector, event reconstruction, and data set.—DEAP-3600 contains (3279 ± 96) kg liquid argon (LAr) in a spherical acrylic vessel (AV) with inner surface area 9.1 m^2, viewed by 255 photomultiplier tubes (PMTs), submerged in a water Cherenkov muon veto (MV). Additional details are described in Refs. [31,32]. The data acquisition and WIMP search analysis are described in Refs. [2,33].

Energy depositions are measured by counting photoelectrons (PEs) in the PMTs resulting from LAr scintillation. PEs are measured by charge division, as in Ref. [33], rather than the Bayesian algorithm in Ref. [2], as the energies and event topologies of interest extend beyond the latter's validation range.

The pulse shape of a waveform $w(t)$ summed over all PMTs is quantified with F_{prompt}, as in Ref. [33],

$$F_{\text{prompt}} = \frac{\int_{-28\ \text{ns}}^{150\ \text{ns}} w(t)dt}{\int_{-28\ \text{ns}}^{10\,000\ \text{ns}} w(t)dt}. \tag{1}$$

F_{prompt} discriminates single-scatter electronic and nuclear recoils [34] and decreases with the number of scatters, separating single and multiple scatters with increasing efficiency at high cross sections.

A second discriminator N_{peaks} is calculated with a peak-finding algorithm based on the waveforms' slope and identifies coincident scintillation pulses in a 10 μs window. This algorithm best identifies multiple-scatter events when the scatters are spread out in time and produce well-separated peaks.

To reduce the volume of data written to disk due to the (3.3 ± 0.3) kBq of ^{39}Ar [2,35], a "prescale" region is defined at low F_{prompt} for 50–565 keV$_{ee}$ energies. Only trigger-level information is recorded for 99% of such events, limiting sensitivity to the lowest cross sections of interest in the present analysis.

This search uses a blind analysis of (813 ± 8) live days of data collected between November 4, 2016 and March 8, 2020, excluding (3 ± 3) μs/trigger to account for DM signals that may be divided between two recorded traces, a 9 d open physics run, and a 6 d muon-coincidence sideband, composed of events within $[-10, 90]$ μs of MV triggers. These open datasets informed the background model and cuts, which were frozen prior to unblinding.

Simulation.—DM is simulated via Monte Carlo with the RAT software [36], built upon GEANT4 [37], in two steps: (1) it is attenuated in the overburden, (2) it is propagated in the detector, simulating optical and data acquisition (DAQ) responses. DM is generated 80 km above Earth's surface with the standard Halo model velocity distribution [38–44] and propagated through Earth to a 1.5 m shell surrounding the AV. DM is boosted into the detector's reference frame for a randomized date, following Refs. [28,45].

Assuming continuous energy loss, the attenuation of DM at position $\vec{r}$ is calculated numerically as [18]

$$\left\langle \frac{dE_\chi}{dt} \right\rangle (\vec{r}) = -\sum_i n_i(\vec{r}) \sigma_{i,\chi} \langle E_R \rangle_i v, \tag{2}$$

with v the lab-frame DM speed, n_i the number density of nuclide i, $\sigma_{i,\chi}$ the DM-nucleus scattering cross section, and $\langle E_R \rangle_i$ the average recoil energy,

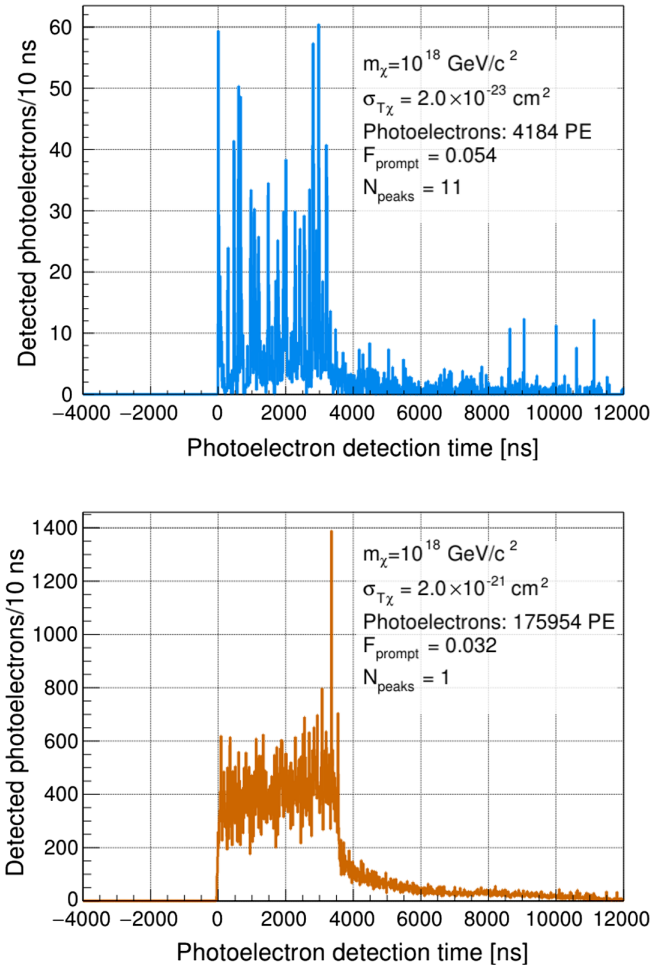

FIG. 1. Example simulated PE time distributions for DM with $m_\chi = 10^{18}$ GeV/c^2 with low and high $\sigma_{T\chi}$.

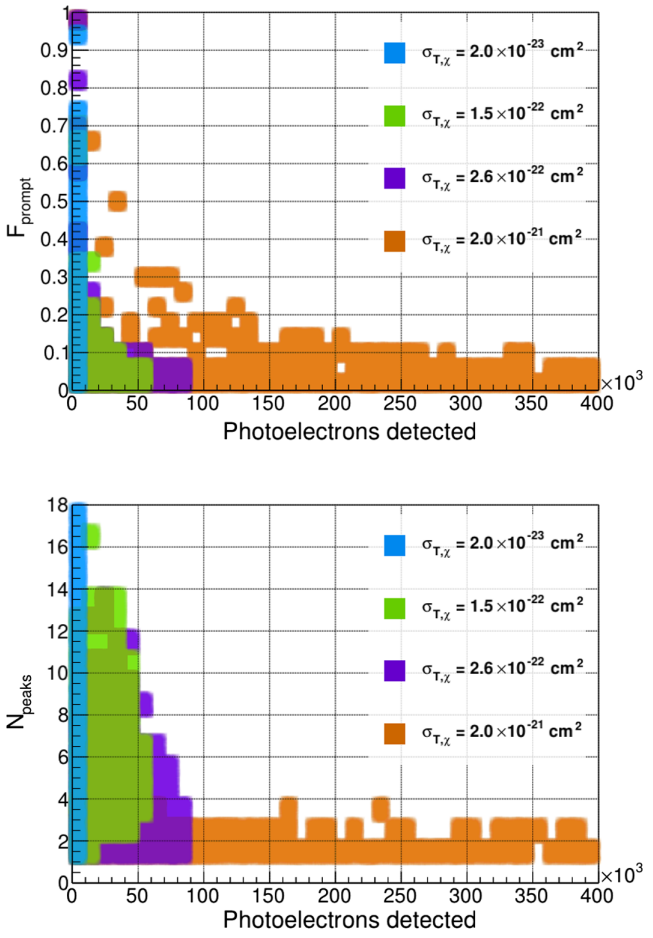

FIG. 2. Simulated F_{prompt} and N_{peaks} distributions for DM with $m_\chi = 10^{18}$ GeV/c^2 for various $\sigma_{T\chi}$.

$$\langle E_R \rangle_i = \frac{1}{\sigma_{i,\chi}} \int_0^{E_i^{\max}} E_R \frac{d\sigma_{i,\chi}}{dE_R} dE_R,$$
$$E_i^{\max} = [4 m_\chi m_i / (m_\chi + m_i)^2] E_\chi, \quad (3)$$

where m_χ and m_i are the DM and nucleus mass, respectively, and $d\sigma_{i,\chi}/dE_R$ is the model-dependent differential scattering cross section (see the section below on Theoretical Interpretations).

The atmospheric density profile is taken from Ref. [46], composed of 79% N_2 and 21% O_2, and Earth's density profile and composition are from Refs. [47,48]. Uncertainties in Earth and atmosphere models negligibly affect the present study. DM is then propagated through DEAP-3600. The detector response is calibrated up to 10 MeV$_{ee}$ using (n, γ) lines from an ^{241}AmBe source, giving a factor of 0.9 ± 0.1 used to scale the simulated PE response.

Figure 1 shows two simulated PE time distributions. At lower nuclear scattering cross sections (denoted $\sigma_{T\chi}$), N_{peaks} counts peaks from individual scatters, which merge at higher $\sigma_{T\chi}$, causing it to lose accuracy. In this regime, the signal energy and duration, typically < 6 μs, depend on the DM speed and track length in LAr, making F_{prompt} an estimate of the fraction of scatters in a 150 ns window around the start of the signal, which decreases at higher $\sigma_{T\chi}$.

Near $\sigma_{T\chi} \simeq 10^{-23}$ cm^2, N_{peaks} grows with increasing $\sigma_{T\chi}$ as the DM scatters more times. As peaks merge, N_{peaks} decreases with $\sigma_{T\chi}$, as seen in Fig. 2. However, F_{prompt} also decreases and narrows as $\sigma_{T\chi}$ grows. For the simulated $\sigma_{T\chi}$, overburden effects have a negligible impact on the DM signal above 10^{12} GeV/c^2 and become significant at lower m_χ.

Analysis and results.—To identify DM over a wide range of energies and scattering lengths, four regions of interest (ROIs) are defined with different cuts on N_{peaks} and F_{prompt}, summarized in Table I. Cuts for ROIs 1–3 mitigate pileup backgrounds that are negligible in ROI 4, which uses minimal cuts that can be evaluated without the full simulation. Doing this allows for constraints on DM-nucleon scattering cross sections $\sigma_{n\chi}$ that are computationally prohibitive to simulate.

TABLE I. Region of interest (ROI) definitions, background expectations μ_b, and observed event counts N_{obs} in the 813 d exposure. A cut rejecting events in a $[-10, 90]$ μs window surrounding each MV trigger is applied to all ROIs; low-level cuts requiring that signals be consistent with bulk LAr scintillation are applied to ROIs 1–3. The upper energy bound on ROI 4 is estimated assuming a constant light yield above 10 MeV_{ee}, the highest energy at which the detector is calibrated.

ROI	PE range	Energy [MeV_{ee}]	$N_{\text{peaks}}^{\text{min}}$	$F_{\text{prompt}}^{\text{max}}$	μ_b	N_{obs}
1	4000–20 000	0.5–2.9	7	0.10	$(4 \pm 3) \times 10^{-2}$	0
2	20 000–30 000	2.9–4.4	5	0.10	$(6 \pm 1) \times 10^{-4}$	0
3	30 000–70 000	4.4–10.4	4	0.10	$(6 \pm 2) \times 10^{-4}$	0
4	70 000–4×10^8	10.4–60 000	0	0.05	$(10 \pm 3) \times 10^{-3}$	0

Backgrounds and selection cuts: The primary backgrounds come from an uncorrelated pileup of signals produced by radioactivity in detector materials, described in Ref. [35]. Correlated backgrounds, such as ^{212}Po α-decays following ^{212}Bi β-decays with a 300 ns half-life, are removed by requiring $N_{\text{peaks}} > 2$ for all energies they may populate.

Pileup was modeled by simulation, validated with a 3.8 h calibration run with an ^{241}AmBe source, which emits neutrons at a (4.6 ± 0.7) kHz rate, and with a 9 d nonblind physics run, testing pileup reconstruction for $N_{\text{peaks}} \leq 4$ up to 7.4 MeV and $N_{\text{peaks}} \leq 5$ up to 2.6 MeV. Simulated N_{peaks} distributions agreed to within 5% in both datasets. ROI 4 relies solely on F_{prompt} for multiscatter detection, since N_{peaks} could not be tested at these energies.

Two low-level cuts in ROIs 1–3 ensure signals are from bulk LAr scintillation: $< 5\%$ of PE must be in PMTs in gaseous Ar, with a DM acceptance of $(99.1 \pm 0.1)\%$, and $< 5\%$ of PE must be in the brightest channel, with a $(86.5 \pm 0.3)\%$ acceptance.

The dominant backgrounds in ROIs 1–3 are from pileup. Pileup rates decrease with energy, allowing the N_{peaks} threshold to accommodate the decreasing accuracy at higher cross sections. Pileup is negligible in ROI 4, where muons produce the dominant backgrounds. Muons are tagged by the veto. Untagged muons are rejected by the F_{prompt} cut, tuned on the muon-coincidence dataset. The background expectation is determined using the flux in Ref. [49].

Table I summarizes cuts and backgrounds in each ROI, defined by the PE range. Energies are provided for illustrative purposes; the listed upper bound on ROI 4 assumes the light yield remains constant above 10 MeV_{ee}, the maximum energy at which the detector is calibrated. Its upper PE bound is consistent with the highest scale at which the DAQ system's performance was tested using calibration data collected with a light injection system. Figure 3 shows the probability of 10^{18} GeV/c^2 DM reconstructing in the PE range for each ROI and passing all cuts.

Results: After finalizing the selection cuts and background model with a total background expectation of 0.05 ± 0.03 across all ROIs, the blinded dataset was opened, revealing zero events. These null results allow any DM model predicting more than 2.3 events across all ROIs to be excluded at the 90% C.L.

The number of events expected in live time T is

$$\mu_s = T \int d^3\vec{v} \int dA \frac{\rho_\chi}{m_\chi} |v| f(\vec{v}) \epsilon(\vec{v}, \sigma_{T\chi}, m_\chi), \quad (4)$$

with local DM density $\rho_\chi = 0.3$ GeV/$(c^2\,\text{cm}^3)$ [39], DM velocity at the detector $\vec{v}$, acceptance ϵ, and surface area A. Equation (4) is evaluated by Monte Carlo simulation, including effects detailed in the section on Simulation, systematic uncertainties on energy and N_{peaks} reconstruction, and Monte Carlo statistical uncertainties.

Theoretical interpretations.—The DM signal and $\sigma_{n\chi}$-$\sigma_{T\chi}$ scaling depend on the DM model. Two composite models are considered. For each model, μ_s is determined at several m_χ and $\sigma_{n\chi}$, and exclusion regions are built accounting for uncertainties as prescribed in Ref. [50]. Upper bounds on m_χ are interpolated with a ρ_χ/m_χ flux scaling; lower bounds are set to the value at which the overburden calculation predicts that 90% of expected DM signals will be below 1 MeV_{ee} after quenching. Upper bounds on $\sigma_{n\chi}$ are set by the lowest simulated values that

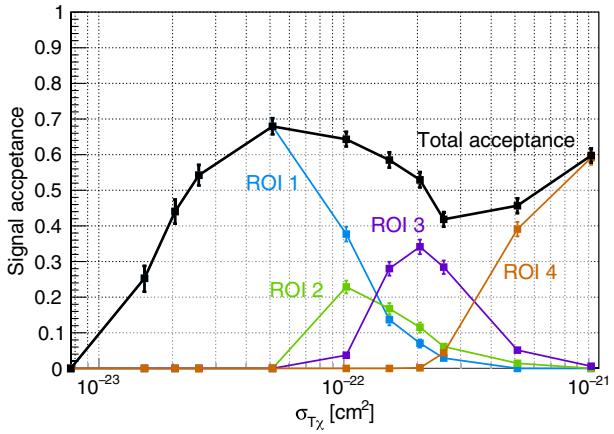

FIG. 3. Probability of DM with $m_\chi = 10^{18}$ GeV/c^2 populating each ROI and surviving all cuts at varying $\sigma_{T\chi}$.

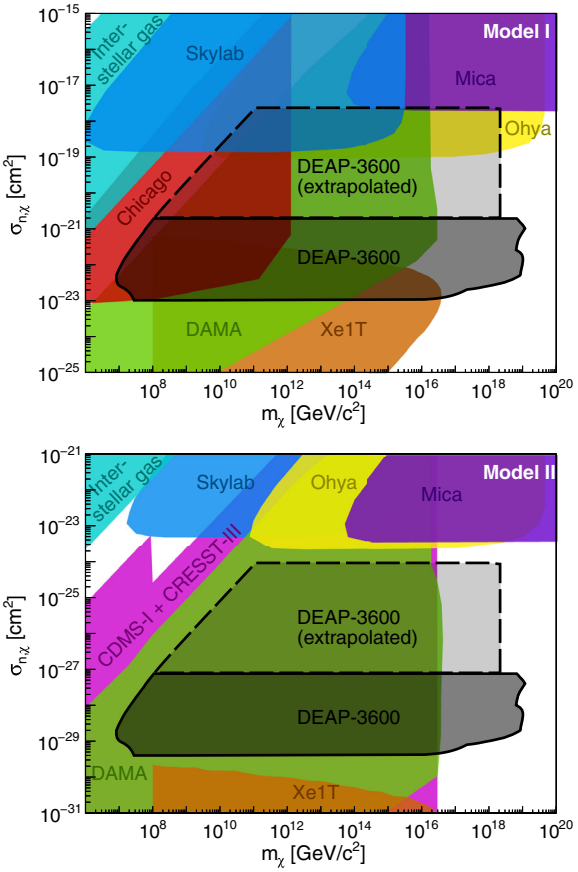

FIG. 4. DM masses m_χ and nucleon scattering cross sections $\sigma_{n\chi}$ excluded by DEAP-3600, for Model I (top) and Model II (bottom). Extrapolated regions exclude dark matter above the highest simulated cross sections. Also shown are other constraints using DAMA [26,51], interstellar gas clouds [52,53], a recast of CRESST and CDMS-I [28], a detector at the University of Chicago [29], a XENON1T single-scatter analysis [30], and tracks in the Skylab and Ohya plastic etch detectors [51], and in ancient mica [54]. Limits from MAJORANA DEMONSTRATOR [30] are not shown as the corresponding regions are already excluded by DAMA and XENON1T.

can be excluded, while lower bounds are limited by the highest $\sigma_{n\chi}$ that were computationally possible to simulate, $\sigma_{n\chi}^{\max}$. At higher $\sigma_{n\chi}$, the continuous scattering approximation and the time of flight in LAr imply a lower bound on the ROI 4 acceptance of 35%. Conservatively treating the probability of reconstructing in ROI 4 as constant above $\sigma_{n\chi}^{\max}$ and scaling the flux as ρ_χ/m_χ, exclusion regions are extrapolated to m_χ consistent with null results. Upper bounds on $\sigma_{n\chi}$ are set to $\sigma_{n\chi}^{\max} \times (\mathrm{PE}_{\max}^{\mathrm{ROI4}}/\mathrm{PE}_{90}^{\mathrm{sim}})$, where $\mathrm{PE}_{\max}^{\mathrm{ROI4}}$ is the upper PE bound of ROI 4 and $\mathrm{PE}_{90}^{\mathrm{sim}}$ is the 90% upper quantile on the PE distribution at $\sigma_{n\chi}^{\max}$. These constraints are labeled "extrapolated" in Fig. 4.

Model I: In this model, DM is opaque to the nucleus, so that the scattering cross section at zero momentum transfer q is the geometric size of the DM regardless of the target nucleus. More generally,

$$\frac{d\sigma_{T\chi}}{dE_R} = \frac{d\sigma_{n\chi}}{dE_R}|F_T(q)|^2, \tag{5}$$

where $F_T(q)$ is the Helm form factor [55]. This scaling may give conservative limits for strongly interacting composite DM [56,57]. The region excluded for this model is shown in Fig. 4 (top). Here (and in the bottom panel) the lower and upper boundaries are flat because, unlike in WIMP searches where these exclusion $\sigma_{T\chi} \propto m_D$ at high DM masses, the cross section sensitivity is only dependent on the detector's multiscatter acceptance. The right-hand boundary is nearly vertical due to the drop in DM flux with increasing m_D; above the notch is the region where Earth overburden is dominated by the crust. On the left-hand boundary $\sigma_{T\chi} \propto m_D$ due to attenuation in the overburden.

Model II: In this scenario the cross section scales as

$$\begin{aligned}\frac{d\sigma_{T\chi}}{dE_R} &= \frac{d\sigma_{n\chi}}{dE_R}\left(\frac{\mu_{T\chi}}{\mu_{n\chi}}\right)^2 A^2|F_T(q)|^2 \\ &\simeq \frac{d\sigma_{n\chi}}{dE_R}A^4|F_T(q)|^2,\end{aligned} \tag{6}$$

where $\mu_{\{n,T\}\chi}$ is the $\{\mathrm{nucleon, target}\}$-DM reduced mass and A is the target mass number. The excluded region is shown in Fig. 4 (bottom).

Equation (6) is the most commonly used scaling, allowing for comparisons with other experiments and with single-scatter constraints. It may arise from nuclear DM models, outlined in Refs. [58,59], which describe a dark nucleus with N_D nucleons of mass m_D and radius r_D, yielding a total mass $m_\chi = N_D m_D$ and radius $R_D = N_D^{1/3} r_D$. For $m_\chi \gg m_T$,

$$\frac{d\sigma_{T\chi}}{dE_R} = \frac{d\sigma_{nD}}{dE_R}N_D^2|F_\chi(q)|^2 A^4|F_T(q)|^2, \tag{7}$$

where σ_{nD} is the nucleon-dark nucleon scattering cross section. To preserve the Born approximation, Eq. (7) is bounded by the geometric cross section:

$$\sigma_{T\chi} \leq \sigma_{\mathrm{geo}}(= 4\pi R_D^2 = 4\pi N_D^{2/3} r_D^2). \tag{8}$$

For dark nuclei of size $R_D \gg 1\,\mathrm{fm}$, we may identify $\sigma_{n\chi} = N_D^2 \sigma_{nD}$ for potentials that give rise to $|F_\chi(q)|^2 \simeq 1$, and Fig. 4 could then constrain such nuclear DM in regions satisfying Eq. (8).

We leave detailed studies of such possibilities to future work.

Summary and scope.—This study uses DEAP-3600 data to derive new constraints on composite DM, including the first direct detection results probing Planck-scale masses. These constraints were obtained through a dedicated analysis of multiple-scatter signals, accounting for the

attenuation that the DM would experience in the laboratory's overburden. The analysis used to achieve these results represents the first study of this kind in a tonne-scale direct detection experiment, extending Planck-scale limits from ancient mica [54] and etched plastic studies [51] to lower cross sections.

The high-mass sensitivity achieved by DEAP-3600 was possible due to its large cross sectional area, which provides a large net to catch dilute DM. As a result, limits were placed on two classes of DM models describing strongly interacting, opaque composites and dark nuclei motivated by the QCD scale with a spherical top-hat potential.

This analysis may be extended to superheavy DM depositing energy via modes other than elastic scattering, (e.g., Ref. [25]), to future LAr, liquid xenon, and bubble chamber detectors, and to large-scale liquid scintillator (e.g., SNO+, JUNO) [18] and segmented detectors (e.g., MATHUSLA) [19].

We gratefully acknowledge fruitful interactions with Javier Acevedo, Joe Bramante, and Alan Goodman. TRIUMF receives federal funding via a contribution agreement with the National Research Council Canada. We thank the Natural Sciences and Engineering Research Council of Canada, the Canadian Foundation for Innovation (CFI), the Ontario Ministry of Research and Innovation (MRI), and Alberta Advanced Education and Technology (ASRIP), Queen's University, the University of Alberta, Carleton University, the Canada First Research Excellence Fund, the Arthur B. McDonald Canadian Astroparticle Research Institute, DGAPA-UNAM (PAPIIT No. IN108020) and Consejo Nacional de Ciencia y Tecnología (CONACyT, Mexico, Grant No. A1-S-8960), the European Research Council Project (ERC StG 279980), the U.K. Science and Technology Facilities Council (STFC) (ST/K002570/1 and ST/R002908/1), the Leverhulme Trust (ECF-20130496), the Russian Science Foundation (Grant No. 21-72-10065), the Spanish Ministry of Science and Innovation (PID2019–109374GB-I00), and the International Research Agenda Programme AstroCeNT (MAB/2018/7) funded by the Foundation for Polish Science (FNP) from the European Regional Development Fund. Studentship support from the Rutherford Appleton Laboratory Particle Physics Division, STFC and SEPNet Ph.D. is acknowledged. We thank SNOLAB and its staff for support through underground space, logistical, and technical services. SNOLAB operations are supported by the CFI and Province of Ontario MRI, with underground access provided by Vale at the Creighton mine site. We thank Vale for their continuing support, including the work of shipping the acrylic vessel underground. We gratefully acknowledge the support of Compute Canada, Calcul Québec, the Centre for Advanced Computing at Queen's University, and the Computation Centre for Particle and Astrophysics (C2PAP) at the Leibniz Supercomputer Centre (LRZ) for providing the computing resources required to undertake this work.

[*]Present address: Nuclear Science Division, Lawrence Berkeley National Laboratory, Berkeley, California 94720, USA.
[†]Present address: Nikhef and the University of Amsterdam, Science Park, 1098XG Amsterdam, Netherlands.
[‡]deap-papers@snolab.ca

[1] N. Aghanim *et al.* (Planck Collaboration), Planck 2018 results VI. Cosmological parameters, Astron. Astrophys. **641**, A6 (2020).
[2] R. Ajaj *et al.* (DEAP Collaboration), Search for dark matter with a 231-day exposure of liquid argon using DEAP-3600 at SNOLAB, Phys. Rev. D **100**, 022004 (2019).
[3] P. Agnes *et al.* (DarkSide Collaboration), DarkSide-50 532-day dark matter search with low-radioactivity argon, Phys. Rev. D **98**, 102006 (2018).
[4] E. Aprile *et al.* (XENON Collaboration), Dark Matter Search Results from a One Ton-Year Exposure of XENON1T, Phys. Rev. Lett. **121**, 111302 (2018).
[5] D. Akerib *et al.* (LUX Collaboration), Results from a Search for Dark Matter in the Complete LUX Exposure, Phys. Rev. Lett. **118** (2017).
[6] X. Cui *et al.* (PandaX-II Collaboration), Dark Matter Results from 54-Ton-Day Exposure of PandaX-II Experiment, Phys. Rev. Lett. **119**, 181302 (2017).
[7] R. Agnese *et al.* (SuperCDMS Collaboration), Results from the Super Cryogenic Dark Matter Search Experiment at Soudan, Phys. Rev. Lett. **120**, 061802 (2018).
[8] C. Amole *et al.* (PICO Collaboration), Dark matter search results from the complete exposure of the PICO-60 C3F8 bubble chamber, Phys. Rev. D **100**, 022001 (2019).
[9] J. Billard, Direct Detection of Dark Matter –APPEC Committee Report, arXiv:2104.07634.
[10] V. Kuzmin and I. Tkachev, Matter creation via vacuum fluctuations in the early Universe and observed ultrahigh energy cosmic ray events, Phys. Rev. D **59**, 123006 (1999).
[11] E. W. Kolb and A. J. Long, Superheavy dark matter through Higgs portal operators, Phys. Rev. D **96**, 103540 (2017).
[12] D. J. H. Chung, E. W. Kolb, and A. Riotto, Superheavy dark matter, Phys. Rev. D **59**, 023501 (1998).
[13] K. Harigaya, T. Lin, and H. K. Lou, GUTzilla dark matter, J. High Energy Phys. 09 (2016) 014.
[14] E. Babichev, D. Gorbunov, and S. Ramazanov, New mechanism of producing superheavy Dark Matter, Phys. Lett. B **794**, 69 (2019).
[15] D. Hooper, G. Krnjaic, and S. D. McDermott, Dark radiation and superheavy dark matter from black hole domination, J. High Energy Phys. 08 (2019) 001.
[16] H. Kim and E. Kuflik, Superheavy Thermal Dark Matter, Phys. Rev. Lett. **123**, 191801 (2019).
[17] J. Bramante, B. Broerman, R. F. Lang, and N. Raj, Saturated overburden scattering and the multiscatter frontier: Discovering dark matter at the Planck mass and beyond, Phys. Rev. D **98**, 083516 (2018).
[18] J. Bramante, B. Broerman, J. Kumar, R. F. Lang, M. Pospelov, and N. Raj, Foraging for dark matter in large volume liquid scintillator neutrino detectors with multi-scatter events, Phys. Rev. D **99**, 083010 (2019).
[19] J. Bramante, J. Kumar, and N. Raj, Dark matter astrometry at underground detectors with multiscatter events, Phys. Rev. D **100**, 123016 (2019).

[20] V. De Luca, A. Mitridate, M. Redi, J. Smirnov, and A. Strumia, Colored dark matter, Phys. Rev. D **97**, 115024 (2018).
[21] A. Coskuner, D. M. Grabowska, S. Knapen, and K. M. Zurek, Direct detection of bound states of asymmetric dark matter, Phys. Rev. D **100**, 035025 (2019).
[22] H. Davoudiasl and G. Mohlabeng, GeV-scale messengers of Planck-scale dark matter, Phys. Rev. D **98**, 115035 (2018).
[23] Y. Bai, M. Korwar, and N. Orlofsky, Electroweak-symmetric dark monopoles from preheating, J. High Energy Phys. 07 (2020) 167.
[24] E. Pontón, Y. Bai, and B. Jain, Electroweak symmetric dark matter balls, J. High Energy Phys. 09 (2019) 011.
[25] B. V. Lehmann, C. Johnson, S. Profumo, and T. Schwemberger, Direct detection of primordial black hole relics as dark matter, J. Cosmol. Astropart. Phys. 10 (2019) 046.
[26] R. Bernabei *et al.*, Extended Limits on Neutral Strongly Interacting Massive Particles and Nuclearites from NaI(Tl) Scintillators, Phys. Rev. Lett. **83**, 4918 (1999).
[27] I. F. M. Albuquerque and L. Baudis, Erratum: Direct Detection Constraints on Superheavy Dark Matter, Phys. Rev. Lett. **90**, 221301 (2003); **91**, 229903(E) (2003).
[28] B. J. Kavanagh, Earth scattering of superheavy dark matter: Updated constraints from detectors old and new, Phys. Rev. D **97**, 123013 (2018).
[29] C. V. Cappiello, J. I. Collar, and J. F. Beacom, New experimental constraints in a new landscape for composite dark matter, Phys. Rev. D **103**, 023019 (2021).
[30] M. Clark, A. Depoian, B. Elshimy, A. Kopec, R. F. Lang, and J. Qin, Direct detection limits on heavy dark matter, Phys. Rev. D **102**, 123026 (2020).
[31] P. A. Amaudruz *et al.* (DEAP Collaboration), Design and construction of the DEAP-3600 dark matter detector, Astropart. Phys. **108**, 1 (2019).
[32] P. A. Amaudruz *et al.* (DEAP Collaboration), In-situ characterization of the Hamamatsu R5912-HQE photomultiplier tubes used in the DEAP-3600 experiment, Nucl. Instrum. Methods Phys. Res., Sect. A **922**, 373 (2019).
[33] P.-A. Amaudruz *et al.* (DEAP Collaboration), First Results from the DEAP-3600 Dark Matter Search with Argon at SNOLAB, Phys. Rev. Lett. **121**, 071801 (2018).
[34] P. Adhikari *et al.* (DEAP Collaboration), Pulse-shape discrimination against low-energy Ar-39 beta decays in liquid argon with 4.5 tonne-years of DEAP-3600 data, Eur. Phys. J. C **81**, 823 (2021).
[35] R. Ajaj *et al.* (DEAP Collaboration), Electromagnetic backgrounds and potassium-42 activity in the DEAP-3600 dark matter detector, Phys. Rev. D **100**, 072009 (2019).
[36] T. Bolton *et al.*, RAT (is an Analysis Tool) User's Guide, https://rat.readthedocs.io (2018).
[37] S. Agostinelli *et al.*, Geant4—a simulation toolkit, Nucl. Instrum. Methods Phys. Res., Sect. A **506**, 250 (2003).
[38] D. Baxter *et al.*, Recommended conventions for reporting results from direct dark matter searches, Eur. Phys. J. C **81**, 907 (2021).
[39] J. D. Lewin and P. F. Smith, Review of mathematics, numerical factors, and corrections for dark matter experiments based on elastic nuclear recoil, Astropart. Phys. **6**, 87 (1996).
[40] M. C. Smith *et al.*, The RAVE survey: Constraining the local Galactic escape speed , Mon. Not. R. Astron. Soc. **379**, 755 (2007).
[41] C. McCabe, The Earth's velocity for direct detection experiments, J. Cosmol. Astropart. Phys. 02 (2014) 027.
[42] R. Schnrich, J. Binney, and W. Dehnen, Local kinematics and the local standard of rest , Mon. Not. R. Astron. Soc. **403**, 1829 (2010).
[43] J. Bland-Hawthorn and O. Gerhard, The galaxy in context: Structural, kinematic, and integrated properties, Annu. Rev. Astron. Astrophys. **54**, 529 (2016).
[44] R. Abuter *et al.* (GRAVITY Collaboration), Improved GRAVITY astrometric accuracy from modeling optical aberrations, Astron. Astrophys. **647**, A59 (2021).
[45] N. Bozorgnia, G. B. Gelmini, and P. Gondolo, Daily modulation due to channeling in direct dark matter crystalline detectors, Phys. Rev. D **84**, 023516 (2011).
[46] National Oceanic and Atmospheric Administration, National Aeronautics and Space Administration, and United States Air Force, US standard atmosphere, NOAA, https://www.ngdc.noaa.gov/stp/space-weather/online-publications/miscellaneous/us-standard-atmosphere-1976/us-standard-atmosphere_st76-1562_noaa.pdf (1976).
[47] J. Lundberg and J. Edsjo, Weakly interacting massive particle diffusion in the solar system including solar depletion and its effect on Earth capture rates, Phys. Rev. D **69**, 123505 (2004).
[48] A. M. Dziewonski and D. L. Anderson, Preliminary reference Earth model, Phys. Earth Planet. Inter. **25**, 297 (1981).
[49] B. Aharmim *et al.*, Measurement of the cosmic ray and neutrino-induced muon flux at the Sudbury neutrino observatory, Phys. Rev. D **80**, 012001 (2009).
[50] R. D. Cousins and V. L. Highland, Incorporating systematic uncertainties into an upper limit, Nucl. Instrum. Methods Phys. Res., Sect. A **320**, 331 (1992).
[51] A. Bhoonah, J. Bramante, B. Courtman, and N. Song, Etched plastic searches for dark matter, Phys. Rev. D **103**, 103001 (2021).
[52] A. Bhoonah, J. Bramante, F. Elahi, and S. Schon, Galactic Center gas clouds and novel bounds on ultralight dark photon, vector portal, strongly interacting, composite, and super-heavy dark matter, Phys. Rev. D **100**, 023001 (2019).
[53] A. Bhoonah, J. Bramante, S. Schon, and N. Song, Detecting composite dark matter with long-range and contact interactions in gas clouds, Phys. Rev. D **103**, 123026 (2021).
[54] J. F. Acevedo, J. Bramante, and A. Goodman, Old rocks, new limits: Excavated ancient mica searches for dark matter, arXiv:2105.06473.
[55] L. Vietze, P. Klos, J. Menéndez, W. C. Haxton, and A. Schwenk, Nuclear structure aspects of spin-independent WIMP scattering off xenon, Phys. Rev. D **91**, 043520 (2015).
[56] M. C. Digman, C. V. Cappiello, J. F. Beacom, C. M. Hirata, and A. H. G. Peter, Not as big as a barn: Upper bounds on dark matter-nucleus cross sections, Phys. Rev. D **100**, 063013 (2019).
[57] R. H. Helm, Inelastic and Elastic Scattering of 187-Mev Electrons from Selected Even-Even Nuclei, Phys. Rev. **104**, 1466 (1956).
[58] E. Hardy, R. Lasenby, J. March-Russell, and S. M. West, Signatures of large composite Dark Matter states, J. High Energy Phys. 07 (2015) 133.
[59] A. Butcher, R. Kirk, J. Monroe, and S. M. West, Can tonne-scale direct detection experiments discover nuclear dark matter?, J. Cosmol. Astropart. Phys. 10 (2017) 035.